I R A M P
8(1), June 2017, pp. 25-35

ISSN: 2229-3159

Molecular Emission Spectroscopy of Cyanide in Laser-induced Plasma

CHRSTIAN G. PARIGGER[1]*, CHRISTOPHER M. HELSTERN[1], GHANESHWAR GAUTAM[2]

[1] *University of Tennessee, University of Tennessee Space Institute, Center for Laser Applications, 411 B.H. Goethert Parkway, Tullahoma, TN 37388-9700, USA*
[2] *Fort Peck Community College, 605 Indian Avenue, Poplar, MT 59255, USA*
** Corresponding author E-mail: cparigge@tennessee.edu (C.G. Parigger)*

ABSTRACT: This work communicates measurements of cyanide (CN) molecular spectra following laser-induced optical breakdown. The time-resolved data are Abel inverted to determine the spatial distributions of the maximum CN signals and to evaluate molecular excitation temperatures. The experiments are conducted in a 1:1 CO_2:N_2 gas mixture contained in a cell kept at atmospheric pressure, and the micro-plasma is generated using 150 mJ, 6 ns Q-switched Nd:YAG laser radiation. A 0.64 m spectrometer disperses the micro-plasma optical emissions, and an intensified charge-coupled device records the data along the wavelength and slit dimensions.

PACS Codes: 52.70.-m, 33.20.-t, 52.25.Jm, 42.62.Fi

Keywords: Plasma diagnostics, molecular spectra, plasma spectroscopy, laser spectroscopy, laser-induced breakdown spectroscopy.

1. INTRODUCTION

The cyanide (CN) molecule has been of interest in a variety of research areas including spectroscopic characterization. CN is evident in many forms in nature and is instrumental in the production of amino acids, lipids, membranes, nucleotides, and proteins. Living organisms use cyanides as a source of nitrogen and plants can use cyanides to defend against disease [1]. Moreover, cyanides can be instrumental in human applications such as gold extraction [2]. Cyanides also occur in industrial processes, such as chemical and drug production, electroplating, iron and steel production, and pesticide and plastic manufacturing [3]. Cyanides are connected to many living organisms and are created through man-made processes, but they are highly toxic, can be lethal and have been used as chemical weapons. To prevent health hazards to humans and to protect the environment, adequate detection of cyanides is imperative. Current detection methods include optical methods, electrochemical methods, mass- spectrometry, gas chromatography, and quartz crystal mass monitors [4]. Although these methods are sufficient in detection of cyanides, molecular emission spectroscopy provides one to measure composition with a minimally invasive approach [5, 6].

Recombination molecular spectra of CN occur subsequent to plasma generation with pulsed laser radiation [7]. The laser-induced dynamics are routinely measured using time-resolved spectroscopy [8]. The recorded laser-induced breakdown spectroscopy (LIBS) studies show atomic and molecular signatures including background contributions that depend on the laser pulse-width in standard ambient temperature and pressure environments [9]. Moreover, to name a couple more LIBS implementations, distribution of molecular species are of interest in elemental mapping and in studies of explosive surrogates [10, 11]. Recent applications of molecular LIBS include laser ablation molecular isotope spectrometry [12]. In terms of measuring molecular spectra with relatively low background contributions from free electron radiation, ultra-short, femtosecond laser-induced breakdown spectroscopy (FLIBS) can be advantageous for CN diagnostics [13]. Femtosecond LIBS has also been applied in measurements of CN to

interpret molecular structure of explosives [14-16], or in remote sensing femtosecond filamentation experiments for atmospheric sensing or filament-induced "fingerprinting" and identification of atmospheric molecules [17]. Combustion applications and femtosecond LIBS measurement of air-methane mixtures include spectroscopy of CN [18]. Bacteria detection with FLIBS reveals CN molecular bands following direct ablation of CN bonds [19], including comparisons of femto- to the classic nanosecond- LIBS [20].

In this work, results from experiments using nanosecond laser spectroscopy are communicated that focus on molecular emission spectroscopy [21]. The interests include cyanide (CN). The CN recombination radiation occurs within the first 100 nanoseconds for laser-induced breakdown in 1:1 CO_2: N_2 gas mixtures when using nanosecond laser pulses to create the laser plasma. Aspects of the analysis including Abel inversions and computational modeling of the plasma are discussed, and how one can make inferences of molecular excitation temperatures. For nominal 6 nanosecond laser pulses and for pulse-energies in the range of 100 to 800 mJ, expansion dynamics and turbulence due to shock phenomena are usually observed. Determination of spatial distributions serves the purpose of investigating the level of homogenous distribution. Local thermodynamic equilibrium is frequently supposed to be valid for diagnostics with atomic and molecular species emission spectroscopy.

2. EXPERIMENTAL DETAILS

The experimental arrangement consists of a set of components typical for time-resolved, laser-induced optical emission spectroscopy, or nanosecond laser-induced breakdown spectroscopy (LIBS) [22]. Primary instrumentation includes a Q-switched Nd:YAG device (Quantel model Q-smart 850) operated at the fundamental wavelength of 1064-nm to produce full-width-at-half-maximum 6-ns laser radiation with an energy of 850 mJ per pulse, a laboratory type Czerny-Turner spectrometer (Jobin Yvon model HR 640) with a 0.64 m focal length and equipped with a 1200 grooves/mm grating, an intensified charge coupled device (Andor Technology model iStar DH334T-25U-03) for recording of temporally and spatially resolved spectral data, a laboratory chamber or cell with inlet and outlet ports together with a vacuum system, electronic components for synchronization, and various optical elements for beam shaping, steering and focusing. The particular arrangement has been used for CN laser-induced optical breakdown spectroscopy, with a selected elements and laser pulses from a Quanta Ray DCR-2 (10) instrument for shadowgraphy studies [23] or for emission spectroscopy of expanding gaseous hydrogen-nitrogn plasma [24].

For the generation of optical breakdown micro-plasma, a singlet lens (Thorlabs model LA1509-C) is used close to the top entrance window of one arm of the chamber containing the 1:1 CO_2:N_2 atmospheric gas mixture (Airgas ultra-high purity N_2 and research grade CO_2). For the 1:2 imaging of the plasma onto the 100 μm spectrometer slit, a fused silica plano-convex lens (Thorlabs model LA4545) is employed. For the CN experiments reported here, the laser pulse energy is attenuated with beamsplitters and apertures from 850 to 150 mJ/pulse. The peak irradiance distributions for a 850 mJ, 6 ns, 1064 nm laser beam have been computed for the Thorlabs LA4545 lens and for f/10 and f/5 focusing [25, 26]. Figures 1 and 2, illustrate the computed radial distributions for f/10 and f/5 focusing, respectively, with the singlet lens positioned at $x = 0$, and the radiation incident from the right. The shallower f/10 focusing reveals about one order of magnitude (or 2^3) larger focal volume than that obtained for f/5 focusing.

In previous experiments, captured shadowgraphs of the breakdown plasma [23] served the purpose of visualizing the plasma expansion when using 850 mJ, 6-ns radiation. One of the objectives of this work includes investigation of spatially resolved CN distribution using Abel inverse transforms along the lines reported for a 9:1 hydrogen-nitrogen atmospheric gas mixture [24]. However, visualization experiments and focal volume computations [25, 26] are helpful for justification of symmetric Abel inverse transform with extensions due to slight spatial asymmetries as for hydrogen and air plasmas [27-29]. Figures 3 and 4 illustrate two shadowgraphs. These shadowgraphs were recorded in standard ambient temperature and pressure laboratory air, revealing vertical stagnation layers that originate from multiple breakdown sites as indicated in the computed focal intensity distribution in Fig. 1.

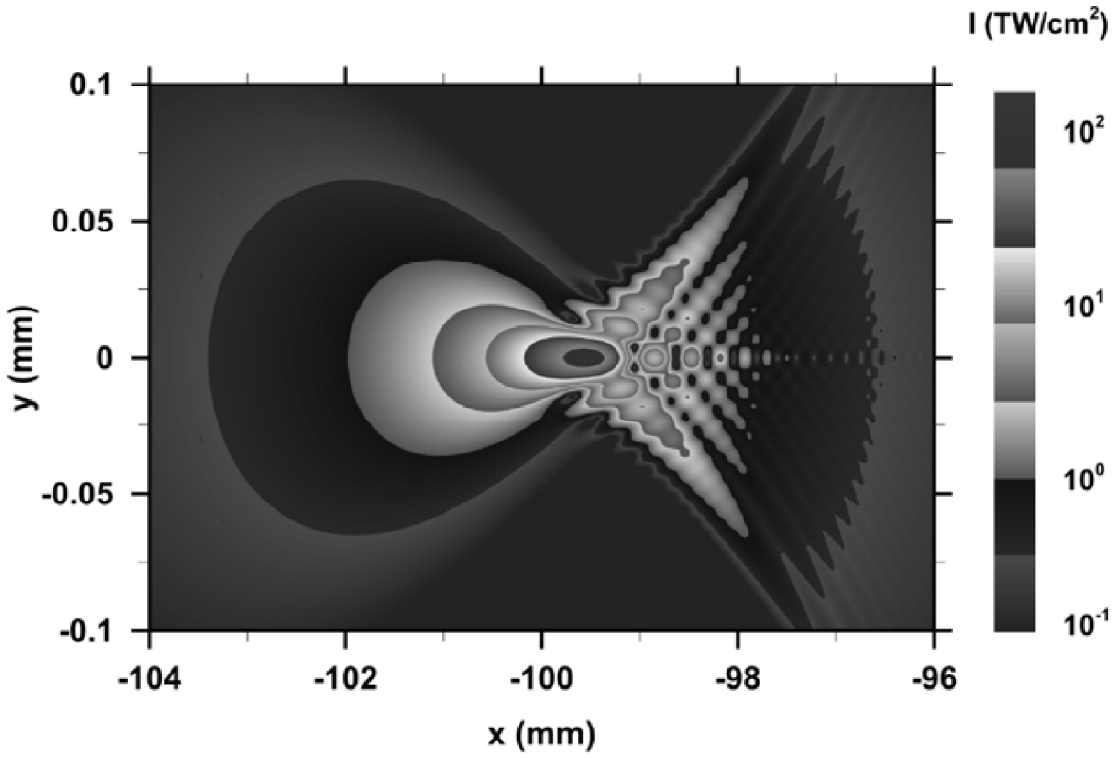

Figure 1: Spatial distribution of 1064-nm laser beam f/10 focusing with the Thorlabs LA4545, 100 mm focal length lens

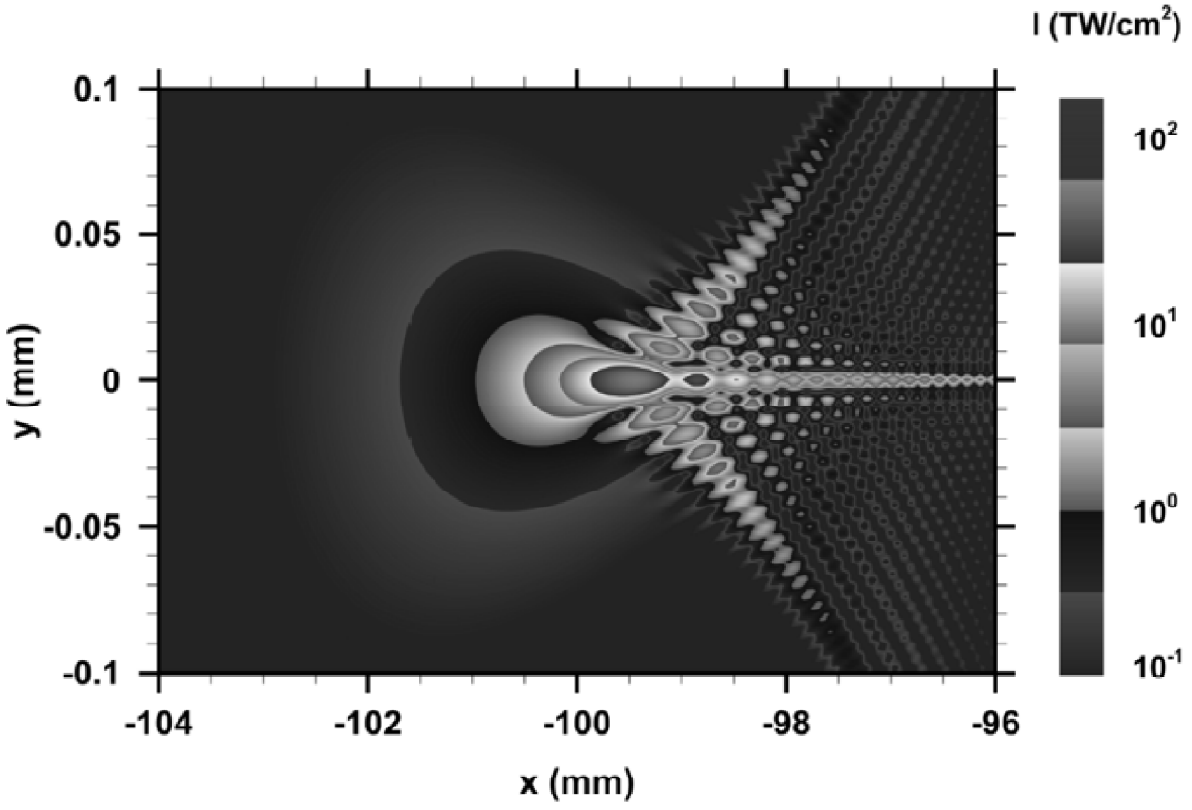

Figure 2: Spatial distribution of 1064-nm laser beam f/5 focusing with the Thorlabs LA4545, 100 mm focal length lens

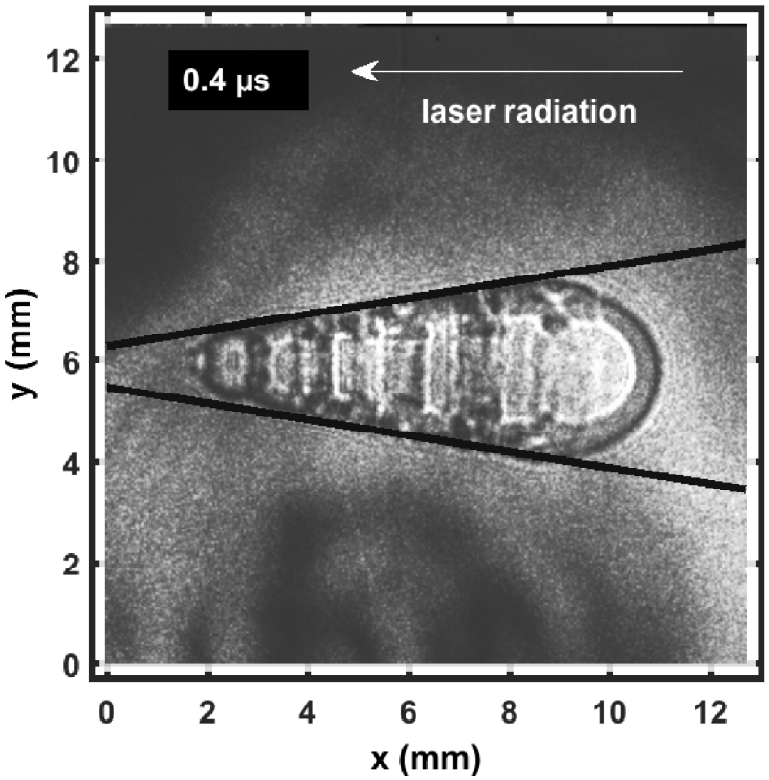

Figure 3: The shock wave maximum expands vertically in excess of Mach 8 (~ 2.5 km/s) for a time delay of 0.4 µs. Higher speeds are measured for shorter time delays from optical breakdown. The lines of slopes ± 6.3 indicate the envelope of the forward shock wave cone

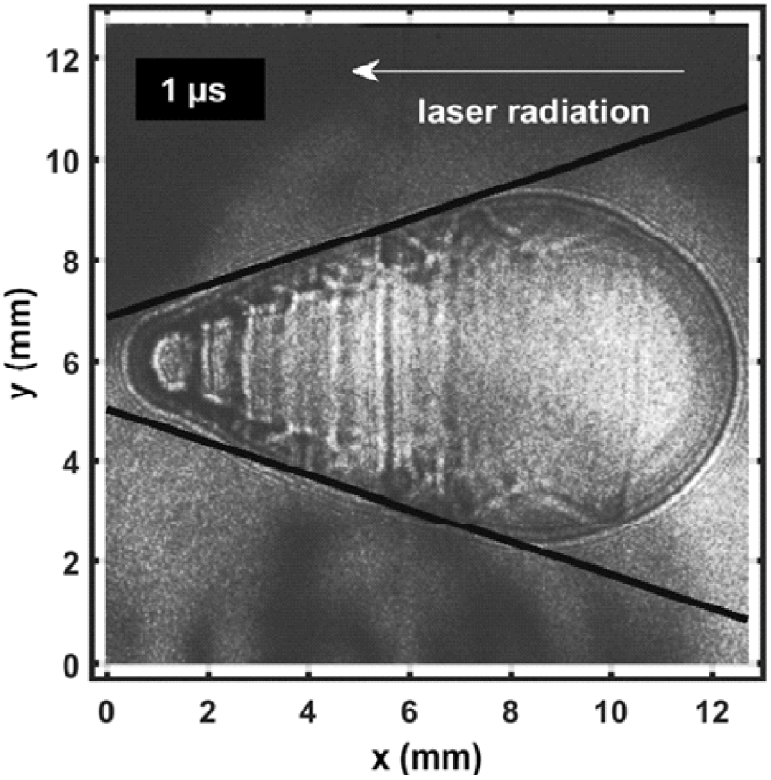

Figure 4: The plasma expands vertically at a speed of Mach 3 (1 km/s) at a time delay of 1 µs. The lines of slopes ± 3 indicate the forward envelopes of the shock wave that primarily grows towards the incoming beam

The laser-supported plasma expansion is consistent with the Taylor-Sedov blast wave model [23, 30]. Increased electron density and temperature occur in the outer region of the plasma kernel [24] as evidenced by the bright-to-dark boundaries that appear to cause multiple reflection inside the shock wave. For the measurement of CN recombination spectra, expansion dynamics are expected to be similar as for the air results indicated in Figs. 3 and 4. However, for an energy/pulse of 150 mJ, a smaller number of breakdown spots are anticipated, leading to a smaller number of stagnation layers than recorded for the 850 mJ/pulse air breakdown events. The expanding "bubble" is also expected to grow to a nearly spherical distribution for shorter time delays with 150 mJ/pulse than for 850 mJ/pulse. Furthermore, the vertical extend is about a factor of 1.4 smaller for 150 mJ pulses than that for 850 mJ pulses, according to the Taylor-Sedov energy dependency [30] for the radius of the spherical expansion. N.b., reported air shadowgraphs [23] for 4 μs time delay and for 850 mJ/pulse optical breakdown in air show a prolate spheroidal distribution that is nearly spherical. This behavior would be consistent with plasma emission measurements in investigations of phenomena near the focal region [27].

3. RESULTS AND DISCUSSION

The experimental series for the measurement of the CN molecular distribution after optical breakdown includes evacuating the cell to a nominal mercury pump vacuum of 10^{-4} Pa (10^{-6} Torr), followed by generating the mixture from ultra-high pure N_2 and research grade CO_2. Optical breakdown was generated inside the chamber at a rate of 10 Hz, with the laser beam focused with f/5 optics from the top, or parallel to the slit. In view of Figures 1 to 4, top would be on the right side and the spectrometer slit would appear horizontally. The detector pixels are binned in 4 tracks along the slit direction, resulting in obtaining 256 spectra for each time delay. In separate recordings, 100 accumulations are collected for 21 time delays. The separate runs included 50 ns, 250 ns, 2500 ns steps for the purpose of determining when CN recombination radiation begins to emanate, what spatial distribution can possibly be measured, and to which extent local thermodynamic equilibrium is established for expanding laser-induced plasma.

Figure 5 displays accumulated raw data for a time delay of 450 ns and a gate width of 125 ns. The vertical axis indicates the slit dimension, the laser beam is focused from the top. With 1:2 imaging, and a pixel resolution of 13.6

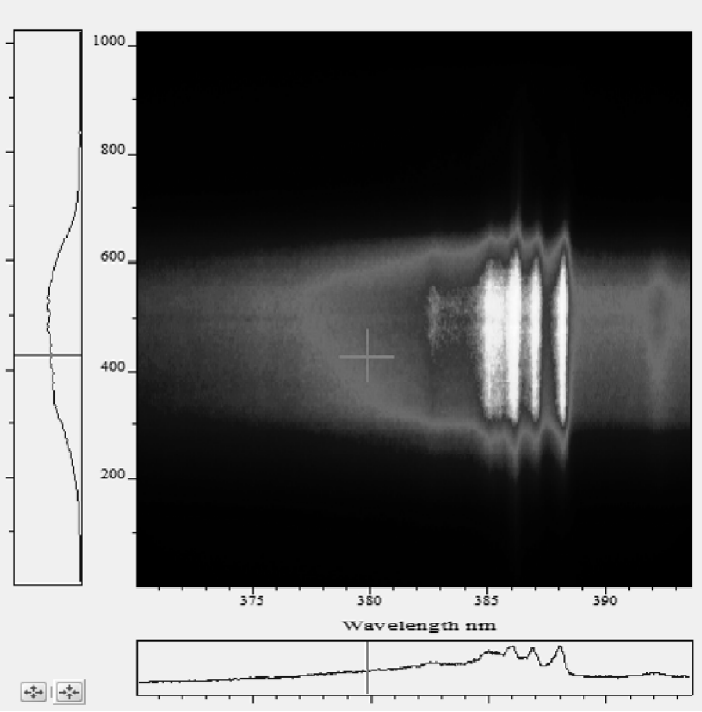

Figure 5: Recorded raw spectra 450 ns after optical breakdown in a 1:1 CO_2:N_2 atmospheric gas mixture

μm, the clearly discernable plasma size in the cell amounts to ~ 3 mm. The figure shows that the CN band heads of the Δv=0 sequence are well-developed, and it also shows an atomic line near 386.2 nm that likely is the carbon CI 193.09 nm atomic line recorded in second order.

In the reported investigations, signatures of the 0-0, 1-1, 2-2, 3-3, 4-4 band heads begin to emanate for time delays of the order of 100 ns from optical breakdown. Moreover, the plasma typically propagates towards the laser side. Figure 6 illustrates the 0.8 mm upward CN-signal propagation in the 370 to 393.5 nm spectral, 4 mm object window during the first 5 microseconds, from a delay of 200 ns to 5200 ns.

The recorded spectra are subjected to Abel inverse transformation to obtain the radial distribution of the plasma. Strictly speaking, radially symmetric profiles are required for Abel inverse transformation. In the analysis of the

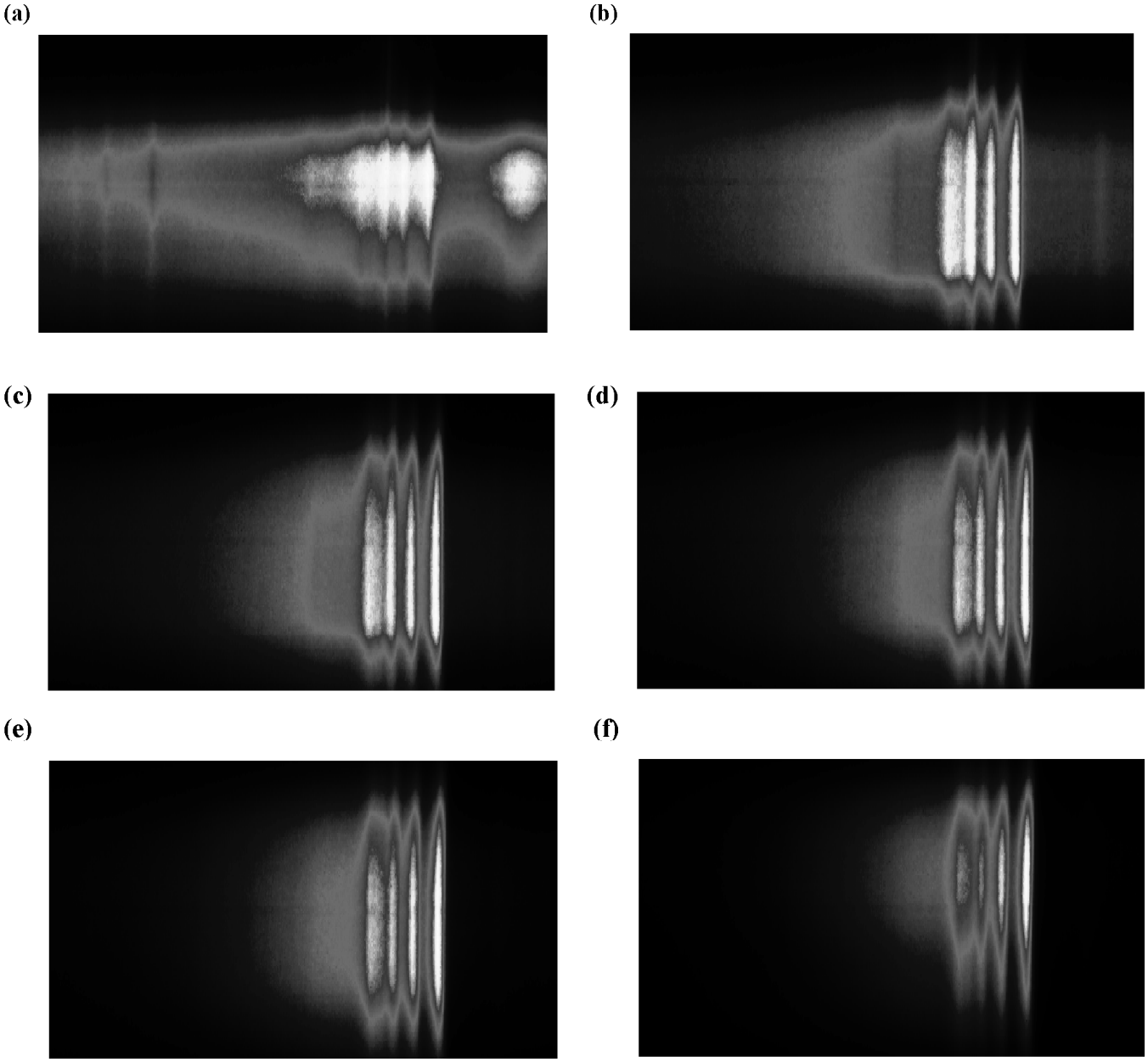

Figure 6: Recorded raw spectra for the 370 to 393.5 nm spectral range (horizontal), 4 mm object range (vertical), and for time delays (a) 200 ns, (b) 700 ns, (c) 1200 ns, (d) 1700 ns, (e) 2200 ns, and (f) 5200 ns. The images are individually scaled from minimum to maximum, showing a vertical CN signal propagation of 0.8 mm in 5 μs.

molecular CN spectra, the same symmetrization methods are applied as for atomic hydrogen spectra [28, 29]. The use of Chebyshev polynomials for the inversion of the integral equation,

$$I(z,\lambda) = 2\int_z^\rho I(r,\lambda)\frac{r}{\sqrt{r^2 - z^2}}dr, \tag{1}$$

allows one to directly invert measured data. The choice of the number of typically 10 polynomials for the inversion [31, 32] is equivalent to the use of a digital filter resulting in the broadening of the computed radial spectra. A smaller number of polynomials would cause smaller spectral resolution. The measured, line-of sight data, $I(z, \lambda)$ along the slit dimension, z, are inverted for each wavelength, λ, to obtain the radial intensity distribution, $I(r, \lambda)$, with the upper limit much larger, $\rho >> R$, than the radius, R, of the plasma. Analysis of asymmetric plasma expansion would require Radon inverse transformations [33].

The radial spectra are computed from the 2-dimensional data that were accumulated with an intensified camera attached to the spectrometer that allows one to resolve spectra along the slit. The recorded data are calibrated and corrected for the system sensitivity using standard lamps. Figures 7 to 9, illustrate the Abel inverted data for time delays of 450 ns, 1200 ns, and 3700 ns, respectively, recorded with a 125 ns gate.

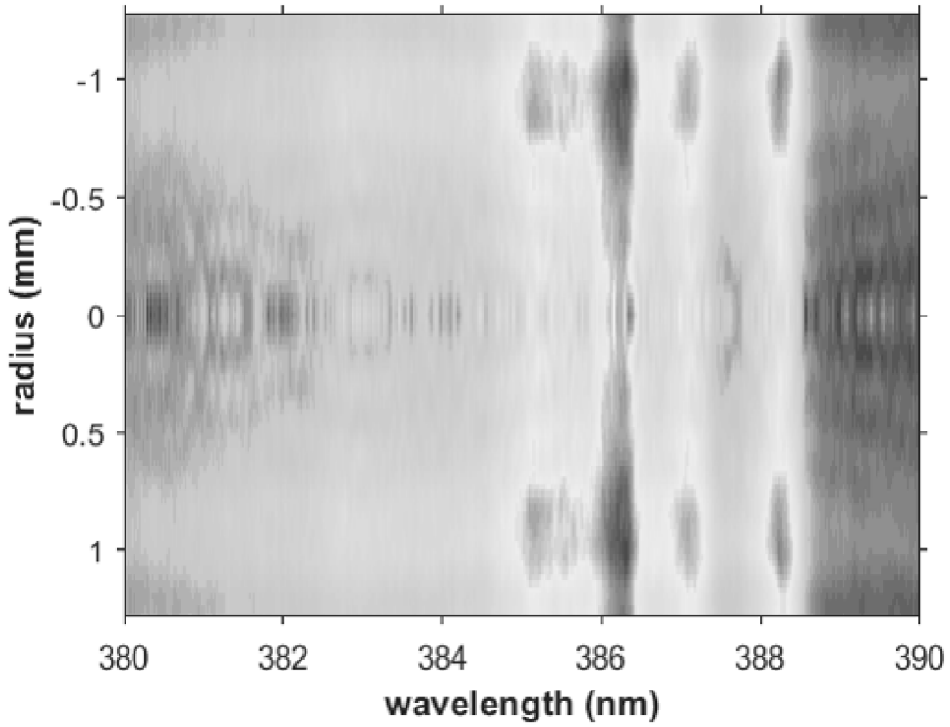

Figure 7: Abel inverted spectra versus radius for a time delay of 450 ns. Near 1 mm, the CN Δv = 0 sequence clearly shows 0-0, 1-1, 3-3 and 4-4 band heads. The line near 386.2 nm that overlaps with the 2-2 band likely corresponds to the CI 193.09 nm atomic line recorded in 2nd order. The CN and atomic line signals are smaller near the center

The electron number density, n_e, can be determined from the Stark full-width at half maxiumum, $\Delta\lambda_{Stark}$, of the line near 386.2 nm that likely corresponds to the CI 193.09 nm atomic carbon line [34] measured in 2nd order,

$$\Delta\lambda_{Stark} = 2w\ n_e\ (10^{16}\ \text{cm}^{-3}) \tag{2}$$

where the width parameter, w, is extrapolated [34, 35] to amount to $w \approx 0.024$ nm. For example, a Stark width of 1 nm recorded in 2nd order (or $\Delta\lambda_{Stark} = 0.5$ nm) near the edges of the 450-ns time delay line-of-sight data (see Figure

5) would yield an electron density of $n_e \sim 10^{17}$ cm^{-3}. However, without further detailed electron density evaluation that would necessitate deconvolution from additional broadening due to choice of typically 10 polynomials in the Abel inversion, Fig. 7 appears to indicate smaller Stark widths that would lead to smaller electron densities near the center.

The recorded and Abel inverted spectra for a time delay of 1200 ns are further analyzed using computational routines previously utilized in the analysis of molecular spectra following laser-plasma generation [7, 36]. Figure 8 displays Abel inverted spectral data and two selected results of fitting computed with measured spectra. At the center, the CN signals are weaker than at 1 mm, indicating a slightly lower temperature than for the 0.85 mm position. There appears to be residual interference from the likely atomic carbon line.

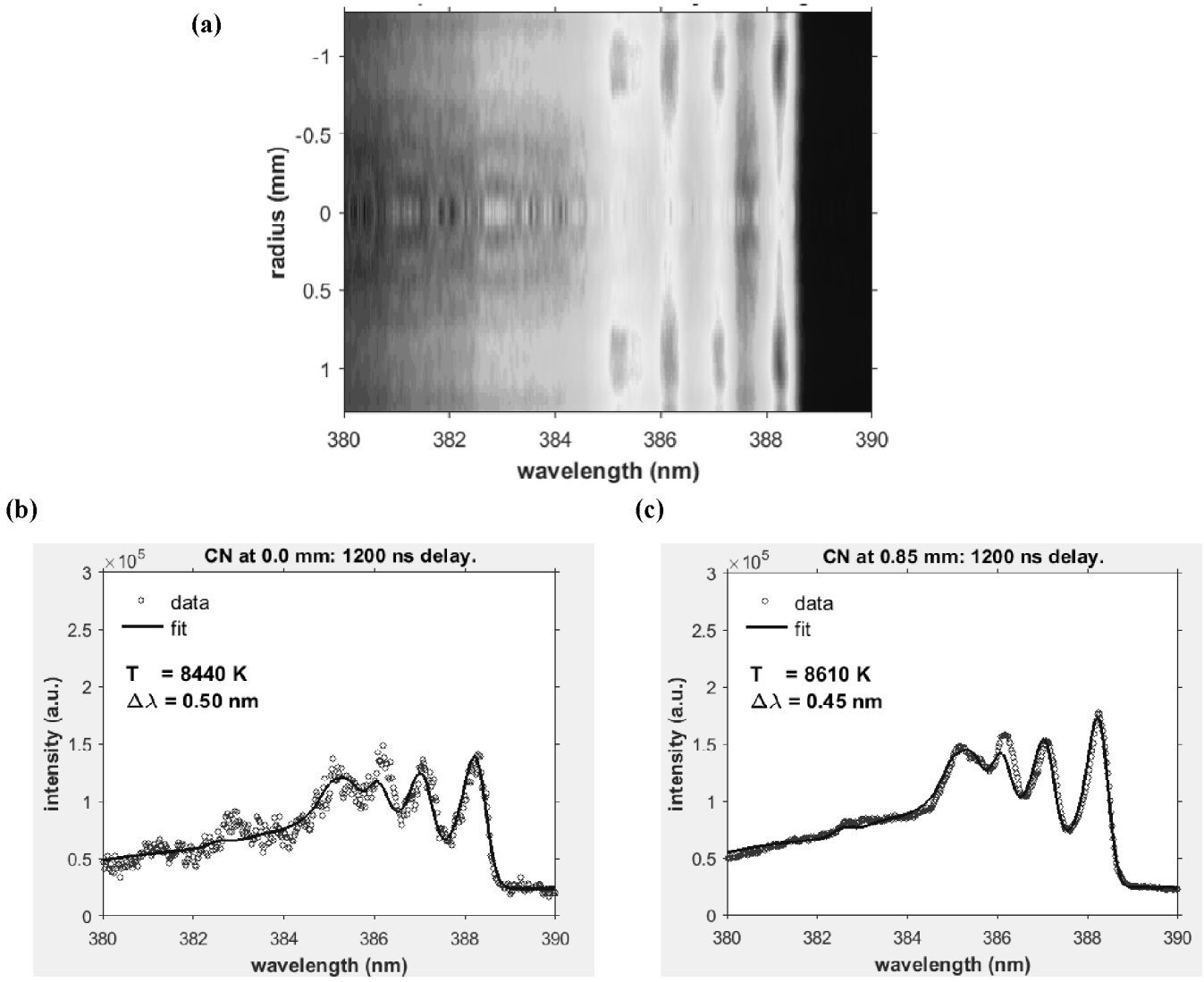

Figure 8: (a) Abel inverted spectra versus radius for a time delay of 1200 ns; Inferred temperature (b) at the center and (c) at the 0.85 mm radial position. There appear to be indications of the likely 2nd order carbon line

For comparison, reasonable signal to noise spectra at 1 mm and at a delay of 3700 ns, show expected lower temperature than that for the 1200 ns time delay. Figure 9 displays a nearly uniform radial distribution of the CN $\Delta v = 0$ sequence.

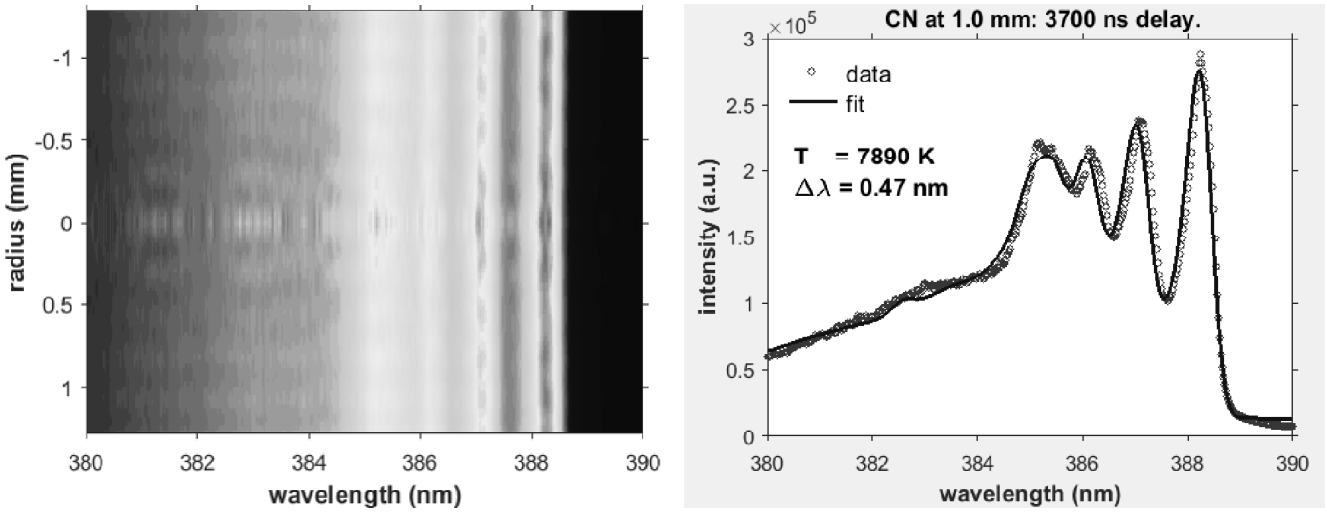

(a) (b)

Figure 9: (a) Abel inverted spectra versus radius for a time delay of 3700 ns; (b) Inferred CN excitation temperature at the 1 mm radial position

One would expect that the CN molecule distribution is close to uniform in chemical equilibrium, as indicated in Figure 9 (a). However, Figs. 7 and 8 (a) reveal stronger signals near the edges of the plasma. In analogy to expansion studies of hydrogen and hydrogen-nitrogen plasma [24, 28, 29], lower signals may occur at the center than at the edge of the plasma kernel due to laser-induced expansion dynamics, particularly during the first few microseconds after optical breakdown. For time delays in the range of 5 to 50 μs, the line-of-sight molecular CN spectra are well developed, and the recorded optical emissions originate from a decreasing volume with increasing gate delay, however further comments and discussion of these spectra are not presented in this work.

In addition, CN recombination radiation signals may be stronger for specific ranges of temperature. Computation of the freely available Chemical Equilibrium with Applications (CEA) code [37] elucidate CN mass fractions versus temperature. Several atoms and molecules including ionic species are part of the CEA computations, but the results for the CN mass fractions are of primary interest in this work. Figure 10 shows the CN distribution for both air and the mixture as function of temperature.

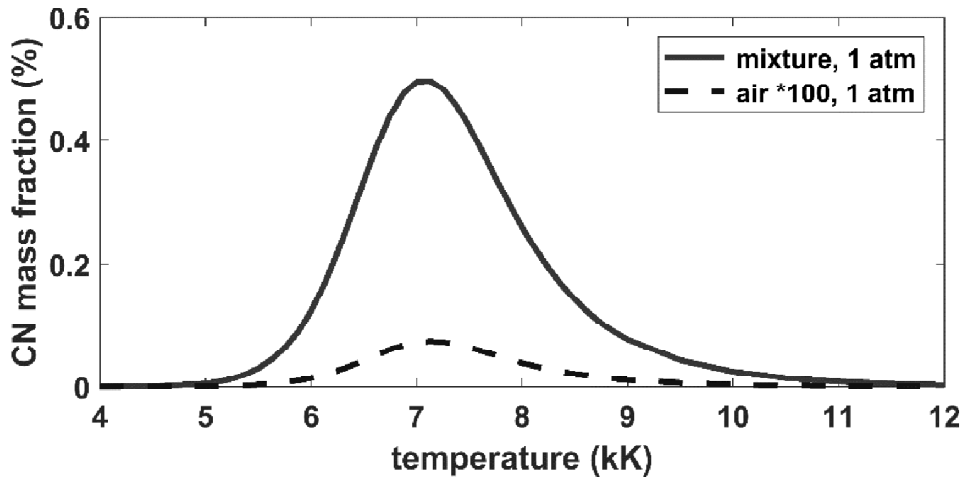

Figure 10: Computed CN mass fraction versus temperature. In chemical equilibrium, CN shows a maximum near 7 kK for the 1:1 atmospheric CO_2: N_2 mixture. CN fractions in air are about 500 × lower than that for the mixture

In view of Figure 10, the recombination signals from the mixture are strongest near 7,000 K. Consequently, one might associate stronger signals in Figs. 7 to 9 with local equilibrium temperatures in the range of 6 to 8 kK. Analysis of the central region of the 450 ns time delay result (see Fig. 8 (a)) reveals a slightly lower temperature at center than that obtained at a radial position of 1 mm, and of course spectroscopic interference from the carbon line in 2nd order is apparent for time delays of 450 and 1200 ns. Line-of-sight data (not further elaborated in this work) would consist of average spectra with contributions from regions at different temperatures. For instance, the molecular CN spectra near the plasma edges, viz. the spectra illustrated in Figs. 6 (a) to 6 (d), show smaller signals near the top and bottom but reveal higher temperatures than in the center portion.

3. CONCLUSIONS

Measured CN recombination spectra following laser-induced optical breakdown show spatial distributions that are affected by expansion dynamics. Stark widths of the atomic line that overlaps with the 2-2 CN band head for time delays in the range of 0.1 to 2 μs would indicate a smaller electron density in the central region of the optical breakdown plasma. As the plasma expands and cools and for time delays of the order of 3 to 5 μs, radiation from excited CN molecules appears evenly distributed and indicates a close to homogeneous temperature for each time-resolved measurement. Slight signal undulations may originate from multiple breakdown spots in the focal volume. Fingerprints of the CN molecule appear typically as early as 50 to 100 ns from optical breakdown. The application of Abel inversion is justified only for radially symmetric light sources, but the shadowgraph studies in air would support symmetrization of the measured data in order to elucidate the spatial dependence. However, detailed studies are in progress. Applications of the chemical equilibrium CEA code indicate that strongest CN signals would occur in the 6,000 to 8,000 K range provided local thermodynamic equilibrium is indeed established.

Acknowledgments

The authors thank for support in part by the Center for Laser Applications at the University of Tennessee Space Institute.

References

[1] P.V. Minorsky, *Plant Physiol.* **155** (2011) 169.

[2] T. Mudder, M. Botz, A. Smith, *Chemistry and Treatment of Cyanidation Wastes*, 2nd ed., Mining Journal Books, London, UK, 2001.

[3] N. Gupta, Balomajumder, V.K.Agarwal, *J. Hazard. Mater.* **176** (2010) 1.

[4] J. Ma, P.K. Dasgupta, *Anal. Chim. Acta* **673** (2010) 117.

[5] R. Noll, *Laser-Induced Breakdown Spectroscopy Fundamentals and Applications*, Springer-Verlag, Heidelberg, DE, 2012.

[6] D. Hahn, N. Omenetto, *Appl. Spectrosc.* **66** (2012) 437.

[7] J.O. Hornkohl, C. Parigger, J.W.L. Lewis, *J. Quant. Spectrosc. Radiat. Transf.* **46** (1991) 405.

[8] A. Kushwaha, R.K. Thareja, Appl. Opt. **47** (2008) G35.

[9] C. G. Parigger, *Spectrochim. Acta Part B* **79-80** (2013) 4.

[10] V. Motto-Ros, Q.L.Ma, S.Grégoire, W.Q.Lei, X.C.Wang, F.Pelascini, F.Surma, V.Detalle, J.Yu, *Spectrochim. Acta Part B* **74-75** (2012) 11.

[11] J. Merten, M. Jones, S. Hoke, S. Allen, *J. Phys.: Conf. Ser.* **548** (2014) 012042.

[12] M. Dong, G.C.-Y. Chan, X. Mao, J.J. Gonzalez, J. Lu, R.E. Russo, *Spectrochim. Acta Part B* **100** (2014) 62.

[13] E.N. Rao, S. Sreedhar, S.P. Tewari, G.M. Kumar, S. V. Rao, in Proceedings *International Conference on Fibre Optics and Photonics,* paper TPo.3, OSA International Conference on Fibre Optics and Photonics, 9–12 December 2012, Chennai, IN.

[14] F.C. De Lucia, J.L. Gottfried, A.W. Miziolek, *Opt. Express* **17** (2009) 419.

[15] E.N. Rao, S. Sunku, S.V. Rao, *Appl. Spectrosc.* **69** (2015) 1342.

[16] E.N. Rao, P. Mathi, S.A. Kalam, S. Sunku, A.K. Singh, B. N. Jagatap, S.V. Rao, *J. Anal. At. Spectrom.* **31** (2016) 737.

[17] Y. Shuai, C.S. Leang, Z. He-Ping, *Chin. Phys. B* **24** (2015) 014208.

[18] M. Kotzagianni, S. Couris, *Chem. Phys. Lett.* **561-562** (2013) 36.

[19] M. Baudelet, L. Guyon, J. Yu, J.-P. Wolf, T. Amodeo, E. Fréjafon, P. Laloi, *J. Appl. Phys.* **99** (2006) 063901.

[20] M. Baudelet, L. Guyon, J. Yu, J.-P. Wolf, T. Amodeo, E. Fréjafon, P. Laloi, *J. Appl. Phys.* **99** (2006) 084701.

[21] A. Thorne, U. Litzén, S. Johansson, *Spectrophysics, Principles and Applications*, Springer, New York, USA, 1999.

[22] D.A. Cremers, L.J. Radziemski, *Handbook of Laser-Induced Breakdown Spectroscopy*, John Wiley & Sons Ltd, USA, 2006.

[23] G. Gautam, C.M. Helstern, K.A. Drake, C.G. Parigger, *Int. Rev. At. Mol. Phys.* **7** (2016) 45.

[24] G. Gautam, C.G. Parigger, C.M. Helstern, K.A. Drake, *Appl. Opt.* **33** (2017) 9277.

[25] C. Parigger, Y. Tang, D.H. Plemmons, J.W.L. Lewis, *Appl. Opt.* **36** (1997) 8214.

[26] C.G. Parigger, Laser-induced breakdown in gases: experiments and simulation, chapter 4 in: A.W. Miziolek, V. Palleschi, I. Schechter (Eds.), *Laser Induced Breakdown Spectroscopy*, Cambridge University Press, New York, USA, 2006.

[27] Y.-L. Chen, J.W.L. Lewis, C. Parigger, *J. Quant. Spectrosc. Radiat. Transf.* **67** (2000) 91.

[28] C.G. Parigger, G. Gautam, D.M. Surmick, *Int. Rev. At. Mol. Phys.* **6** (2015) 43.

[29] C.G. Parigger, D.M. Surmick, G. Gautam, *J. Phys.: Conf. Ser.* **810** (2017) 012012.

[30] G.I. Taylor, *Proc. Roy. Soc. A* **201** (1950) 175.

[31] G. Pretzler, *Z. Naturforsch.* **46a** (1991) 639–641.

[32] G. Pretzler, H. Jäger, T. Neger, H. Philipp, and J. Woisetschläger, *Z. Naturforsch.* **47a** (1992) 955.

[33] S. Eschlbçck-Fuchs, A. Demidov, I. Gornushkin, T. Schmid, R. Rçssler, N. Huber, U. Panne, J. Pedarnig, *Spectrochim. Acta Part B* **123** (2016) 59.

[34] M. Dackman, Laser-Induced Breakdown Spectroscopy for Analysis of High Density Methane-Oxygen Mixtures, Master's Thesis, University of Tennessee, Knoxville, TN, 2014.

[35] H.R. Griem, *Spectral Line Broadening by Plasmas,* Academic Press, New York, USA, 1974.

[36] C.G.Parigger, A.C.Woods, D.M.Surmick, G. Gautam, M.J.Witte, J.O.Hornkohl, *Spectrochim. Acta Part B* **107** (2015) 132.

[37] B.J. McBride, S. Gordon, *Computer Program for Calculating and Fitting Thermodynamic Functions*, NASA RP-1271, 1992; on-line 2005 version at *https://cearun.grc.nasa.gov/* (last accessed November 26, 2017).